Received: 30 March 2022 | Accepted: 7 June 2022

DOI: 10.1002/asna.20224019

Astronomische Nachrichten

ORIGINAL ARTICLE

Optical spectroscopy of the Be/black hole binary MWC 656 - interaction of a black hole with a circumstellar disc

Radoslav K. Zamanov[1,*] | Kiril A. Stoyanov[1] | Dragomir Marchev[2] | Nikolay A. Tomov[1] | Uwe Wolter[3] | Michael F. Bode[4,5] | Yanko M. Nikolov[1] | Stefan Y. Stefanov[1] | Alexander Kurtenkov[1] | Georgi Y. Latev[1]

[1]Institute of Astronomy and National Astronomical Observatory, Bulgarian Academy of Sciences, Sofia, Bulgaria

[2]Department of Physics and Astronomy, Shumen University "Episkop Konstantin Preslavski", Shumen, Bulgaria

[3]Hamburger Sternwarte, Universität Hamburg, Hamburg, Germany

[4]Astrophysics Research Institute, Liverpool John Moores University, Liverpool, UK

[5]Office of the Vice Chancellor, Botswana International University of Science and Technology, Palapye, Botswana

Correspondence
Radoslav K. Zamanov, Institute of Astronomy and National Astronomical Observatory, Bulgarian Academy of Sciences,
72 Tsarigradsko Shose, 1784 Sofia, Bulgaria.
Email: rkz@astro.bas.bg

Funding information
Bulgarian National Science Fund, Grant/Award Number: KP-06-H28/2 08.12.2018

Abstract

We present new spectroscopic observations of the Be/black hole binary MWC 656 obtained during the period 2015–2021. We measure the equivalent width of H_α (EW_α), H_β (EW_β), and the distance between the peaks of H_α (ΔV_α), H_β (ΔV_β), and FeII ($\Delta V_{\rm FeII}$) lines. Combining new and old data, we find that: (1) the density of the circumstellar disc of MWC 656 (ΔV_α versus EW_α diagram) is similar to the Be stars. For the Be stars, we find the relation $\Delta V_\beta = 0.999\Delta V_\alpha + 62.4$ km s^{-1}, and the position of MWC 656 corresponds to the average behavior of the Be stars. This means that the presence of the black hole does not change the overall structure of the circumstellar disc; (2) the periodogram analysis indicates modulation of EW_α with a period 60.4 ± 0.4 days, which is identical to the binary orbital period. The maxima of EW_α and EW_β are around periastron (phase zero); (3) around orbital phase zero, ΔV_β and ΔV_{FeII} decrease by about 30 km s^{-1}. This suggests that we observe an increase of the circumstellar disc size induced by the periastron passage of the black hole and that the entire circumstellar disc pulsates with the orbital period with relative amplitude of 10–20%. The observations also indicate, that the reason for the black hole in MWC 656 to be in deep quiescence is a very low efficiency of accretion ($\sim 2 \times 10^{-6}$).

KEYWORDS

stars: emission-line, Be, binaries: spectroscopic, stars: individual: MWC 656, stars: winds, outflows, X-rays: binaries

1 | INTRODUCTION

The Be/X-ray binaries consist of a rapidly rotating Be star and a compact object accreting material from the circumstellar decretion disc. The primary has a mass > 8 $M_\odot$ and the compact object can be a neutron star or a black hole. The orbital periods are in the range 10–400 days (Reig 2011). The common understanding is that the neutron stars have a canonical mass of about 1.4 $M_\odot$ (Heiselberg & Pandharipande 2000). Recent studies support the idea that the neutron stars in high-mass X-ray binaries display a relatively large range in mass – from the theoretical lower mass limit of 1 $M_\odot$ up to over 2 $M_\odot$ (Nice et al. 2005; Shibata et al. 2019). The masses of the black holes in the high-mass X-ray binaries are in the range 5–14 $M_\odot$ (Shao & Li 2020). The Be/X-ray binaries are a product of the evolution of a binary containing two moderately massive stars,

which undergoes mass transfer from the originally more massive star toward its companion (Negueruela 2007; Pols et al. 1991). The angular momentum transfer that accompanies the mass transfer onto the initially less massive star is the most likely reason for the rapid rotation of the Be star (Peters et al. 2013). The eccentricities of the Be/X-ray binaries with orbital periods less than 150 days are from 0 to 0.5 (Brown et al. 2018; Brown et al. 2019) and are caused by the natal kick to the compact object and mass loss during the supernova explosion that formed it (e.g., Brandt & Podsiadlowski 1995; Martin et al. 2009).

The mass donors (primaries) of the Be/X-ray binaries are emission-line Be stars. The Be stars are fast-rotating B-type stars with luminosity class III-V which, at some point in their lives, have shown spectral lines in emission (Porter & Rivinius 2003). The material expelled from the equatorial belt of a rapidly rotating Be star forms an outwardly diffusing gaseous, dust-free Keplerian disc (Rivinius et al. 2013). In the optical band, the most significant observational characteristic of Be stars is the variable emission lines. These emission lines trace the presence of the surrounding decretion disc, and may appear and disappear together with the disc during the star's life. Moving along the orbit, the compact object passes close to this disc, and sometimes may go through it. The gravitational force and tidal effect cause perturbations in the disc structure. This circumstellar disc feeds the accretion disc around the compact object and/or interacts with its relativistic wind and its magnetosphere.

MWC 656 (HD 215227) is the first binary system discovered to contain a black hole orbiting a Be star (Casares et al. 2014). It is associated with the transient γ-ray source AGL J2241 + 4454 (Lucarelli et al. 2010). MWC 656 is not included in the list of the confirmed γ-ray binaries because it was only occasionally detected by the AGILE observatory at GeV energies and not yet detected in the TeV domain (Aleksić et al. 2015). The donor star in the system is a B1.5–2 III star with a mass in the range 10–16 $M_\odot$ (Casares et al. 2014). The orbital period of the system is 60.37 ± 0.04 days, detected by optical photometry (Williams et al. 2010) and confirmed by radial velocity measurements (Casares et al. 2012). The spectral observations reveal the presence of a HeII λ4686 Å emission line produced by the accretion disc around the compact object. The analysis of the radial velocity of this line provides a secondary mass 3.8–6.9 $M_\odot$, which proves that the compact object is a stellar mass black hole (Casares et al. 2014).

Here we present optical spectroscopy of MWC 656 from 2011 to 2021 and discuss the emission lines formed in the circumstellar disc and the orbital influence of the black hole on the Be star disc.

2 | OBSERVATIONS

We have obtained 73 optical spectra of MWC 656 on 50 nights secured with the ESpeRo Echelle spectrograph (Bonev et al. 2017) on the 2.0 m RCC telescope of the Rozhen National Astronomical Observatory, Bulgaria. Six of them are used in our previous studies. Some emission line profiles of H_α, H_β and FeII 5316 of MWC 656 are presented in Figure 1. The spectra are normalized to the local continuum and a constant is added to each spectrum. In this figure are plotted only 9 spectra. Twenty-seven spectra were secured with the HEROS spectrograph on the 1.2 m TIGRE telescope (Schmitt et al. 2014) in the astronomical observatory La Luz in Mexico during the period April 2019–January 2020. In addition, we also use 65 red and 36 blue spectra [analyzed in Casares et al. 2012] from the archive of the 2.0 m Liverpool Telescope (Steele et al. 2004). These spectra were obtained using the Fiber-fed RObotic Dual-beam Optical Spectrograph [FRODOSpec; Morales-Rueda et al. 2004] during the period April–July 2011.

From the Rozhen spectra we measure the following parameters: the equivalent width of the H_α line (EW_α), the distance between the peaks of the following emission lines H_α (ΔV_α), H_β (ΔV_β), FeII 5316 (ΔV_{5316}), FeII 5197 (ΔV_{5197}), and FeII 6435 (ΔV_{6435}). To measure the position, we applied Gaussian fitting at the top of the peak. From the TIGRE spectra are measured EW_α, EW_β, and ΔV_β, and from the Liverpool Telescope spectra are measured EW_α and EW_β. Because in the wings of H_β, traces of the broad photospheric absorption are visible, in all the cases EW_β is the equivalent width of that part of the emission line which is above the level of the local continuum. The measurements are given in a few tables – Table 1 gives EW_α, Table 2 gives ΔV_α, Table 3 gives EW_β, Table 4 gives ΔV_β, and Table 5 gives $\Delta V_{\rm Fe}$. The typical errors are ±5 % for EW_α, ±7 % for EW_β, ±3 km s^{-1} for ΔV_β, and ±5 km s^{-1} for $\Delta V_{\rm Fe}$.

3 | RESULTS

In only a few cases in our spectra does the H_α emission line show two peaks. H_β and Fe II lines are double peaked on all the spectra. This is not surprising, as H_α is optically thick and its shape is affected by radiative transfer effects (e.g., Hummel 1994a, 1994b) and by the presence of the black hole (see Section 3.4).

3.1 | Disc structure

In Figure 2 we plot the distance between the peaks of H_α normalized with the stellar rotation versus EW_α.

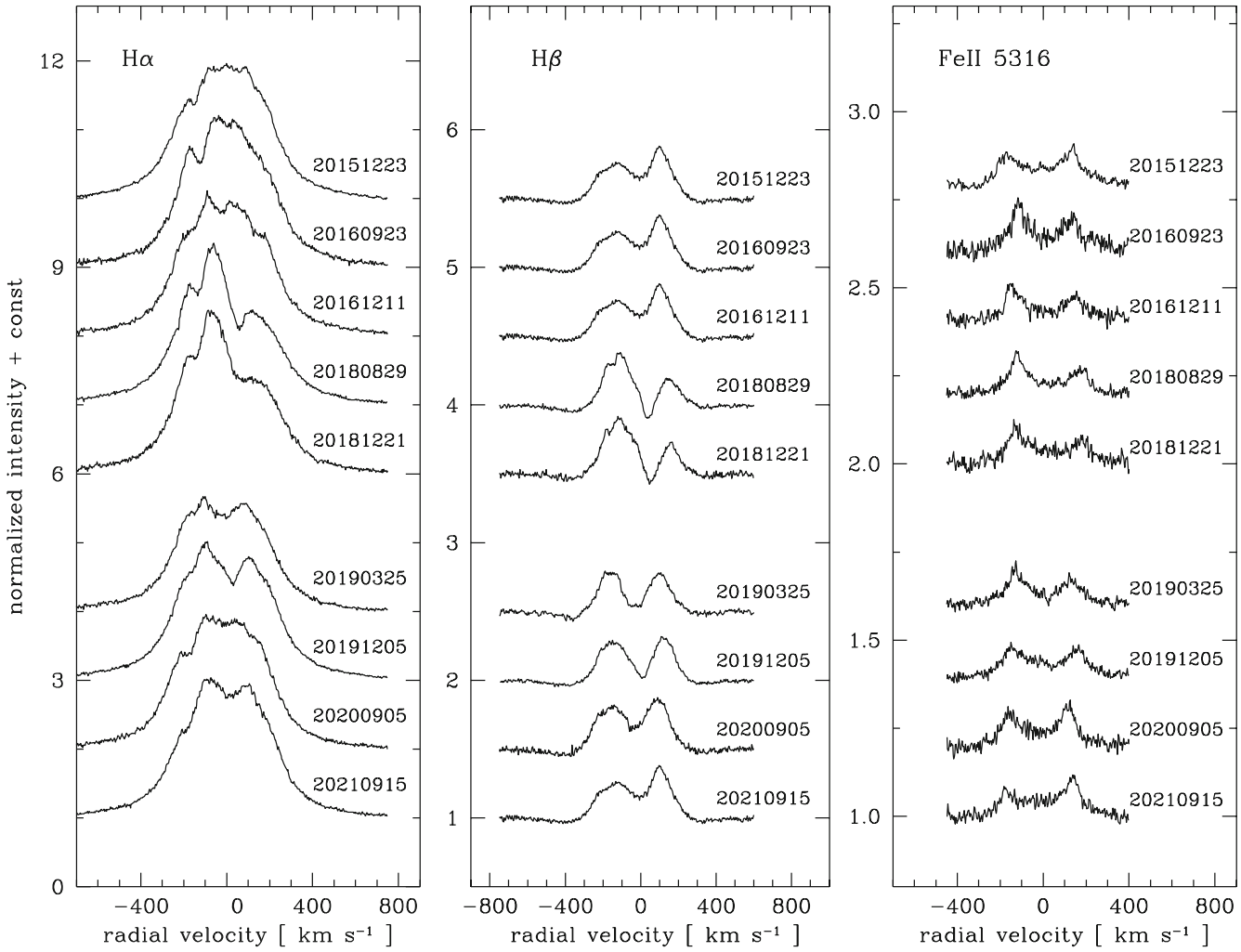

FIGURE 1 Variable profiles of the emission lines H_α, H_β and FeII 5316 of MWC 656. The date of observations is in the format YYYYMMDD

These two parameters correlate in the Be stars, representing the fact that EW_α increases as the disc grows. The black open circles are data for Be stars taken from Andrillat (1983), Hanuschik (1986), Hanuschik et al. (1988), Dachs et al. (1992), Slettebak et al. (1992) and Catanzaro (2013). The red plus signs are our measurements of MWC 656 when the H_α emission is double peaked.

In Figure 2, we see that MWC 656 lies within the Be stars population. The points lie close to and slightly above the average line. For the projected rotational velocity of the primary component of MWC 656 we used $v \sin i = 313$ km s^{-1} (Zamanov et al. 2021). The use of $v \sin i = 330$ km s^{-1} (Casares et al. 2014), will move the points slightly down and they will be even closer to the average line. The vertical scatter of the points on this diagram is due to the density in the disc (see Section 5.2 in Hanuschik et al. 1988), which implies that the density in the circumstellar disc in MWC 656 is similar to the average of that in Be star discs.

In Figure 3 we plot ΔV_β versus ΔV_α. For this figure we used the data from Hanuschik et al. (1988), our values for Be/γ-ray binaries (Zamanov et al. 2016) and our measurements on the spectra of Catanzaro (2013). For the Be stars, Hanuschik et al. (1988) find that the peak separations of H_β and H_α emission lines follow approximately the relation $\Delta V_\beta \approx 1.8 \Delta V_\alpha$. Using more data, we find that this relation is not valid above $\Delta V_\alpha \approx 200$ km s^{-1}. Using a linear fit in the form $y = a + bx$, we find the relation:

$$\Delta V_\beta = 0.998(\pm 0.008)\Delta V_\alpha + 62.4(\pm 1.0) \text{ km s}^{-1}, \quad (1)$$

where ΔV_β and ΔV_α are in km s^{-1}. This relation is valid up to 360 km s^{-1}. As expected, there is a very strong correlation between these two quantities, with correlation coefficient 0.91 and significance 10^{-10}. The position of MWC 656 is very close to the average behavior of other Be stars.

TABLE 1 EW_α of MWC 656. In the Table are given HJD, EW_α, and the telescope Ro, Rozhen; TI, TIGRE; LT, Liverpool telescope

HJD-2450000	EW_α[Å]		HJD	EW_α		HJD	EW_α		HJD	EW_α	
7209.45820	22.58	Ro	8889.22715	20.49	Ro	8778.5527	20.80	TI	5746.53928	21.65	LT
7238.51411	23.05	Ro	9071.39779	21.77	Ro	8787.6122	21.05	TI	5746.54302	21.22	LT
7239.43916	22.73	Ro	9071.41932	20.65	Ro	8798.6807	22.15	TI	5747.58250	21.10	LT
7380.23985	21.70	Ro	9071.44710	19.41	Ro	8807.6478	21.25	TI	5747.58623	21.22	LT
7381.22172	21.44	Ro	9072.43325	19.42	Ro	8816.5657	20.88	TI	5748.52945	21.56	LT
7382.17444	21.48	Ro	9072.45478	19.67	Ro	8825.5471	20.55	TI	5748.53318	21.18	LT
7383.23478	21.87	Ro	9072.47701	19.35	Ro	8833.6131	20.85	TI	5750.54930	21.50	LT
7384.24999	22.69	Ro	9097.33973	22.15	Ro	8842.5554	22.60	TI	5750.55303	21.42	LT
7418.24782	23.16	Ro	9097.36264	21.79	Ro	8843.5732	21.39	TI	5751.53900	21.58	LT
7478.55794	24.22	Ro	9098.39114	21.11	Ro	8865.5772	21.61	TI	5751.54273	21.71	LT
7558.39879	22.02	Ro	9098.41336	21.53	Ro	5675.70236	20.80	LT	5752.51401	21.40	LT
7561.42121	20.28	Ro	9101.27107	21.49	Ro	5675.70609	20.56	LT	5752.51773	21.75	LT
7654.52680	23.86	Ro	9101.29259	21.83	Ro	5691.71744	22.45	LT	5753.49472	22.23	LT
7655.36222	23.26	Ro	9101.38912	22.52	Ro	5691.72118	22.38	LT	5753.49844	22.41	LT
7734.23018	21.66	Ro	9126.32609	19.63	Ro	5697.64370	21.69	LT	5756.57664	21.95	LT
8267.52316	21.56	Ro	9162.22581	21.42	Ro	5697.64743	21.90	LT	5756.58037	22.21	LT
8274.55830	19.58	Ro	9162.25984	21.98	Ro	5700.70738	22.65	LT	5759.49896	21.82	LT
8360.48052	20.79	Ro	9162.29109	21.46	Ro	5700.71112	22.98	LT	5759.50269	22.07	LT
8361.44027	19.65	Ro	9277.14227	21.79	Ro	5703.68169	21.11	LT	5760.52770	21.65	LT
8362.52294	21.14	Ro	9278.14016	21.85	Ro	5703.68542	20.95	LT	5760.53142	21.24	LT
8363.53339	21.36	Ro	9358.51178	19.95	Ro	5712.71041	21.86	LT	5761.52250	22.03	LT
8364.45841	21.45	Ro	9359.52225	20.11	Ro	5712.71414	21.67	LT	5761.52623	22.36	LT
8473.34350	21.62	Ro	9360.50008	20.25	Ro	5712.71414	21.72	LT	5762.54107	22.14	LT
8474.22399	21.65	Ro	9420.35524	20.97	Ro	5718.70789	23.55	LT	5762.54480	22.20	LT
8567.62876	19.83	Ro	9420.38997	21.30	Ro	5718.71162	23.64	LT	5765.51294	21.30	LT
8625.51303	20.80	Ro	9473.43785	21.66	Ro	5722.70951	24.25	LT	5765.51667	21.71	LT
8625.55539	20.55	Ro	9474.34828	21.11	Ro	5722.71323	24.05	LT	5767.46415	20.69	LT
8648.45537	21.71	Ro	9509.27856	21.43	Ro	5729.63596	22.47	LT	5767.46788	20.79	LT
8648.46301	20.93	Ro	8601.9518	20.60	TI	5729.63968	22.55	LT	5771.49588	22.24	LT
8648.47065	20.11	Ro	8613.9492	23.13	TI	5730.66177	22.02	LT	5771.49969	22.16	LT
8682.42632	23.22	Ro	8622.9631	21.73	TI	5730.66551	22.03	LT			
8682.46869	23.33	Ro	8631.9509	20.52	TI	5731.61273	21.73	LT			
8683.44166	22.64	Ro	8648.9298	20.65	TI	5731.61645	21.77	LT			
8683.48403	22.93	Ro	8661.8871	20.95	TI	5732.60107	21.18	LT			
8714.34399	20.74	Ro	8671.8757	20.98	TI	5732.60480	21.13	LT			
8715.41556	20.41	Ro	8690.7678	20.25	TI	5736.66567	20.90	LT			
8716.38644	20.61	Ro	8699.7475	20.38	TI	5736.66940	21.07	LT			
8718.34346	21.67	Ro	8699.8523	20.25	TI	5738.64170	21.77	LT			
8803.41370	24.21	Ro	8708.8044	19.57	TI	5738.64543	21.84	LT			
8823.24312	21.79	Ro	8720.7572	21.33	TI	5740.65714	20.89	LT			

TABLE 1 (Continued)

HJD-2450000	EW_α[Å]		HJD	EW_α		HJD	EW_α		HJD	EW_α	
8833.22997	21.39	Ro	8729.7546	20.80	TI	5740.66086	20.97	LT			
8833.23830	21.23	Ro	8739.6932	22.68	TI	5744.66896	21.38	LT			
8859.24002	24.60	Ro	8749.6375	21.54	TI	5744.67277	21.10	LT			
8859.27613	25.10	Ro	8759.5988	20.76	TI	5745.59023	21.25	LT			
8859.30390	25.80	Ro	8768.6880	20.77	TI	5745.59396	21.27	LT			

TABLE 2 ΔV_α

HJD-2450000	ΔV_α [km s^{-1}]	
8567.62876	175.2	Ro
8625.51314	190.2	Ro
8625.55570	181.8	Ro
8683.44186	157.3	Ro
8683.48414	142.9	Ro
8823.24315	201.1	Ro
9473.43827	165.2	Ro

TABLE 3 EW_β

HJD-2450000	EW_β [Å]		HJD-2450000	EW_β [Å]	
5675.69897	1.232	LT	8613.94918	1.791	TI
5691.71464	1.294	LT	8622.96308	1.648	TI
5697.64122	1.394	LT	8631.95087	1.310	TI
5700.70501	1.376	LT	8648.92984	1.314	TI
5703.67952	1.165	LT	8661.88711	1.481	TI
5712.70860	1.607	LT	8671.87572	1.644	TI
5718.70660	1.887	LT	8690.76781	1.303	TI
5722.70830	2.018	LT	8699.74746	1.406	TI
5729.63535	1.705	LT	8699.85233	1.515	TI
5730.66109	1.476	LT	8708.80439	1.092	TI
5731.61209	1.254	LT	8720.75715	1.505	TI
5732.60065	1.303	LT	8729.75464	1.703	TI
5736.66551	1.109	LT	8739.69322	2.091	TI
5738.64154	1.197	LT	8749.63753	1.618	TI
5740.65725	1.230	LT	8759.59880	1.471	TI
5744.66932	1.122	LT	8768.68801	1.424	TI
5745.59068	1.212	LT	8778.55269	1.546	TI
5746.53979	1.159	LT	8787.61219	1.684	TI
5747.58307	1.239	LT	8798.68068	1.774	TI

TABLE 3 (Continued)

HJD-2450000	EW_β [Å]		HJD-2450000	EW_β [Å]	
5748.53010	1.204	LT	8807.64779	1.582	TI
5750.55008	1.259	LT	8816.56567	1.361	TI
5751.53967	1.262	LT	8825.54706	1.335	TI
5752.51489	1.273	LT	8833.61308	1.388	TI
5753.49567	1.204	LT	8843.57318	1.560	TI
5756.57774	1.215	LT	8865.57720	1.669	TI
5759.50029	1.176	LT			
5760.52910	1.204	LT			
5761.52397	1.228	LT			
5762.54258	1.250	LT			
5765.51464	1.324	LT			
5767.46596	1.464	LT			
5771.49789	1.642	LT			
6076.70430	1.722	LT			
6081.70660	2.096	LT			
6082.68514	1.984	LT			
6083.60974	1.825	LT			

TABLE 4 ΔV_β. In the first part are given Rozhen, in the second TIGRE data

HJD-2400000		HJD		HJD	
Rozhen	ΔV_β [km s^{-1}]	Rozhen	ΔV_β	TIGRE	ΔV_β
57209.45820	254.3	58859.24002	239.5	58622.96308	251.5
57238.51411	243.4	58859.27613	241.4	58631.95087	242.0
57239.43916	245.5	58859.30390	258.0	58648.92984	271.4
57380.23985	261.1	58889.22715	274.0	58661.88711	259.2
57381.22172	271.1	59071.39779	252.8	58671.87572	188.1
57382.17444	274.4	59071.41932	261.6	58690.76781	247.9
57383.23478	270.0	59071.44710	252.5	58699.74746	258.7
57384.24999	260.3	59072.43325	253.9	58699.85233	270.4
57418.24782	237.0	59072.45478	256.6	58708.80439	282.7
57478.55794	241.4	59072.47701	262.8	58720.75715	260.8
57558.39879	254.0	59098.39114	244.1	58729.75464	246.0
57561.42121	270.5	59098.41336	234.9	58739.69322	219.5
57654.52680	238.5	59101.27107	247.0	58749.63753	252.0
57655.36222	232.5	59101.29259	242.5	58759.59880	264.9
57734.23018	264.6	59101.38912	246.0	58768.68801	257.3
58267.52316	252.7	59126.32609	260.9	58778.55269	260.3

TABLE 4 (Continued)

HJD-2400000		HJD		HJD	
Rozhen	ΔV_β [km s^{-1}]	Rozhen	ΔV_β	TIGRE	ΔV_β
58274.55830	248.3	59162.22581	235.6	58787.61219	249.7
58360.48052	267.7	59162.25984	237.6	58798.68068	264.7
58361.44027	276.4	59162.29109	238.0	58807.64779	243.8
58362.52294	265.7	59277.14227	256.7	58816.56567	249.6
58363.53339	268.8	59278.14016	249.9	58825.54706	274.8
58364.45841	264.4	59358.51178	263.0	58833.61308	268.9
58473.34350	271.2	59359.52225	257.9	58843.57318	241.9
58474.22399	275.7	59360.50008	263.3	58865.57720	246.7
58567.62876	255.7	59420.38997	255.5		
58625.51303	260.7	59473.43785	227.3		
58625.55539	259.4	59474.34828	241.5		
58648.45537	257.4				
58648.46301	265.3				
58648.47065	261.1				
58682.42632	248.0				
58682.46869	253.1				
58683.44166	244.1				
58683.48403	244.4				
58714.34399	268.1				
58715.41556	264.7				
58716.38644	269.5				
58718.34346	260.7				
58803.41370	251.0				
58823.24312	270.0				
58833.22997	266.9				
58833.23830	267.9				

TABLE 5 ΔV_{Fe}

HJD-2400000		HJD		HJD		HJD	
FeII 5316	ΔV_{Fe} [km s^{-1}]	FeII 5316	ΔV_{Fe}	FeII 6433	ΔV_{Fe}	FeII 5197	ΔV_{Fe}
57209.45820	276.1	58889.22715	291.4	58715.41556	293.5	58833.23830	287.4
57238.51411	249.4	59071.39779	270.9	58716.38644	292.5	58859.27613	248.1
57239.43916	257.9	59071.41932	277.7	58803.41370	287.8	58889.22715	265.9
57380.23985	299.6	59071.44710	279.9	58823.24312	310.5	59071.41932	300.1
57381.22172	299.6	59072.43325	266.7	58833.23830	295.2	59072.45478	271.4
57382.17444	292.5	59072.45478	266.5	59072.45478	280.1	59072.47701	287.6

TABLE 5 (Continued)

HJD-2400000		HJD		HJD		HJD	
FeII 5316	ΔV_{Fe} [km s^{-1}]	FeII 5316	ΔV_{Fe}	FeII 6433	ΔV_{Fe}	FeII 5197	ΔV_{Fe}
57383.23478	289.6	59072.47701	268.0	59101.29259	249.9	59098.39114	260.7
57384.24999	289.7	59098.39114	254.2	59162.22581	241.1	59098.41336	263.8
57418.24782	238.9	59098.41336	266.4	59360.50008	292.1	59101.27107	252.9
57478.55794	251.2	59101.27107	251.0	59473.43785	293.9	59101.29259	263.0
57558.39879	289.3	59101.29259	243.4	59474.34828	264.9	59126.32609	281.5
57561.42121	282.2	59101.38912	252.6	59509.27856	280.1	59162.22581	249.8
57654.52680	244.9	59126.32609	279.8			59162.25984	243.2
57655.36222	240.1	59162.22581	233.9	FeII 5197		59162.29109	241.5
57734.23018	290.1	59162.25984	240.8	57209.45820	285.6	59277.14227	273.5
58267.52316	299.9	59162.29109	250.2	57238.51411	270.1	59358.51178	281.0
58274.55830	264.6	59277.14227	248.7	57239.43916	262.4	59359.52225	299.5
58360.48052	289.7	59278.14016	259.0	57380.23985	283.6	59360.50008	280.8
58361.44027	285.2	59358.51178	279.8	57381.22172	300.5	59473.43785	288.7
58362.52294	292.3	59359.52225	295.2	57382.17444	284.6	59474.34828	284.5
58363.53339	279.7	59360.50008	277.8	57383.23478	293.6	59509.27856	286.3
58364.45841	261.7	59420.38997	279.5	57384.24999	285.6		
58473.34350	293.0	59473.43785	295.5	57418.24782	263.3		
58474.22399	294.5	59474.34828	287.7	57561.42121	289.8		
58567.62876	251.3	59509.27856	297.0	57655.36222	250.3		
58625.51303	262.6			57734.23018	313.5		
58625.55539	261.4	FeII 6433		58360.48052	299.5		
58648.45537	287.6	57209.45820	277.1	58361.44027	291.1		
58648.46301	300.2	57381.22172	296.6	58362.52294	283.8		
58648.47065	294.8	57383.23478	299.7	58363.53339	268.4		
58682.42632	266.8	57384.24999	285.0	58364.45841	267.8		
58682.46869	245.0	57418.24782	260.5	58473.34350	290.2		
58683.44166	269.0	57655.36222	261.0	58474.22399	298.4		
58683.48403	263.0	57734.23018	304.1	58567.62876	277.8		
58714.34399	285.8	58274.55830	279.7	58625.51303	250.2		
58715.41556	290.6	58360.48052	298.1	58648.47065	298.9		
58716.38644	291.2	58361.44027	304.4	58683.44166	259.5		
58718.34346	264.8	58362.52294	276.1	58714.34399	290.6		
58803.41370	259.3	58363.53339	277.6	58715.41556	286.9		
58823.24312	280.3	58567.62876	276.9	58716.38644	285.1		
58833.22997	291.6	58648.47065	306.0	58718.34346	282.7		
58833.23830	283.2	58682.42632	276.0	58803.41370	242.9		
58859.24002	271.2	58683.44166	271.7	58823.24312	291.7		
58859.27613	270.9	58714.34399	312.2	58833.22997	270.3		

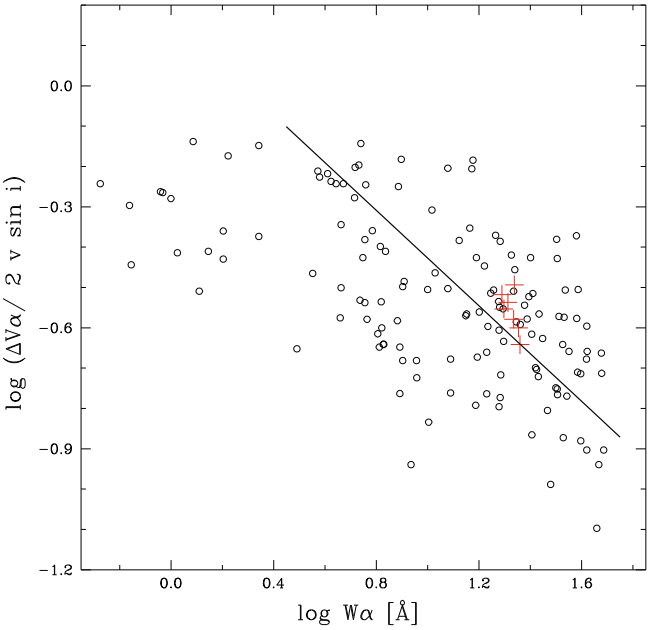

FIGURE 2 ΔV_α versus EW_α. The black circles are the Be stars (see text) and the red plusses are our observations of MWC 656. The solid line is the average behavior of Be stars

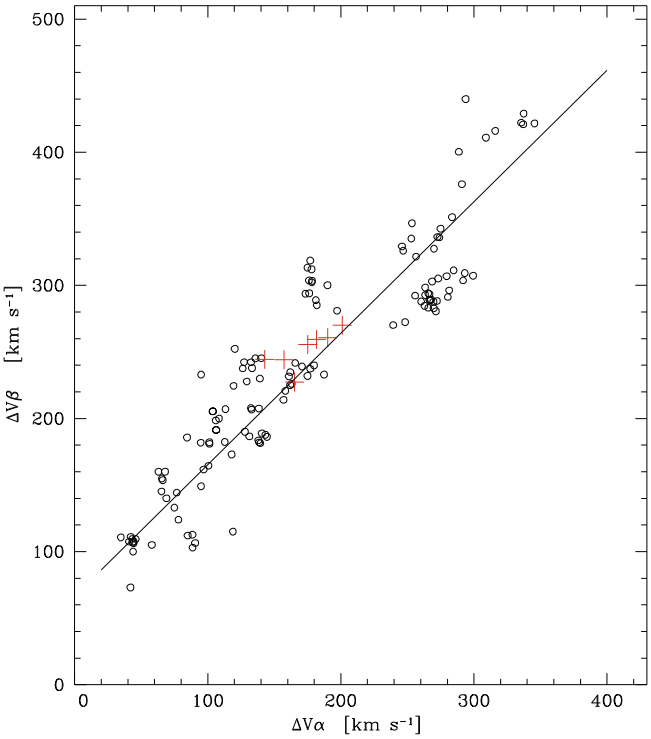

FIGURE 3 ΔV_β versus ΔV_α for Be stars (black circles). The red crosses are our data for MWC 656. The solid line is the linear fit $\Delta V_\beta = 0.987\ \Delta V_\alpha + 66.9$ km s^{-1}

The behavior of MWC 656 in Figures 2 and 3, indicates that the circumstellar disc is not strongly perturbed by the presence of the orbiting black hole and its overall structure is similar to the discs in the classical Be stars.

3.2 | Disc size

For emission line profiles coming from a Keplerian disc, the peak separation (ΔV) can be regarded as a measure of the outer radius ($R_{\rm disc}$) of the emitting disc (e.g., Huang 1972):

$$\Delta V = 2 \sin i \sqrt{GM_1/R_{\rm disc}}, \tag{2}$$

where G is the gravitational constant, M_1 is the mass of the Be star and $\sin i$ is the inclination of the disc to the line of sight. The projected rotational velocity ($v \sin i$) of a Be star can be expressed as

$$v \sin i = (1 - \varepsilon) \sin i \sqrt{GM_1/R_1}, \tag{3}$$

where R_1 is the radius of the Be star, and ε is a dimensionless parameter for which we adopt $\varepsilon = 0.1 \pm 0.1$. The term $(1 - \varepsilon)$ represents the fact that the Be stars are rotating below the critical value (Porter & Rivinius 2003). We obtain the following expression for R_{disc}:

$$R_{\rm disc} = R_1 \left(\frac{2v \sin i}{(1 - \varepsilon)\Delta V} \right)^2, \tag{4}$$

which relies on the assumptions that: (a) the disc is complanar with the equatorial plane of the Be star, (b) the Be star rotates below the critical rate, and (c) the line profile shape is dominated by kinematics, and radiative transfer does not play a role. Radius estimation through this method is a good approximation for symmetric profiles with two peaks.

There is also a connection between $R_{\rm disc}$ and EW_α. We will use it in the form (see also Zamanov et al. 2013):

$$R_{\rm disc} = R_1 (1 - \varepsilon) 0.467 EW_\alpha^{1.184} \tag{5}$$

where ε is the same dimensionless parameter as in Equation 3. A similar approach (with slightly different coefficients) was applied by Coe et al. (2006) and by Monageng et al. (2017). Equation 5 gives us the possibility to estimate disc radius using measurements of EW_α and is applicable even in cases when the H_α emission line does not display a double-peaked profile, but something different—single peak, triple peak profile, etc.

Following Table 1, we find that EW_α is in the range $19.4 \leq EW_\alpha \leq 25.8$ Åwith average value 21.6 ± 1.1 Å. Using Equation 5, $R_1 = 8.8$ R$_\odot$ (Zamanov et al. 2021), and

from the measurements of EW_α, we estimate the size of the circumstellar disc in MWC 656 to be in the range $123 \leq R_{\rm disc} \leq 174$ R$_\odot$, with average value $R_{\rm disc} = 141 \pm 8$ R$_\odot$.

The distance between the peaks of H_β is in the range $214 \leq \Delta V_\beta \leq 282$ km s^{-1}, with average value 255 ± 14 km s^{-1}. Using Equation 4 and our measurements of ΔV_β, we find that the size of the disc visible in H_β emission is in the range $54 \leq R_{\rm disc}(H\beta) \leq 93$ R$_\odot$, with average value $R_{\rm disc}(H\beta) = 66 \pm 8$ R$_\odot$.

The distance between the peaks of the FeII 5316 line is in the range $237 \leq \Delta V_{\rm FeII5316} \leq 305$ km s^{-1}, with average value 274 ± 19 km s^{-1}. The distance between the peaks of the FeII 5197 line is in the range $242 \leq \Delta V_{\rm FeII5197} \leq 314$ km s^{-1}, with average value 277 ± 18 km s^{-1}. Finally, the distance between the peaks of the FeII 6433 line is in the range $243 \leq \Delta V_{\rm FeII5197} \leq 312$ km s^{-1}, with average value 285 ± 18 km s^{-1}. As can be expected, the three FeII lines have similar behavior. Using Equation 4 and our measurements of $\Delta V_{\rm FeII}$, we find that the size of the disc visible in FeII emission lines is in the range $43 \leq R_{\rm disc}({\rm FeII}) \leq 76$ R$_\odot$, with average value $R_{\rm disc}({\rm FeII}) = 56 \pm 8$ R$_\odot$. The calculated disc sizes indicate that H_α emission traces the outer parts of the disc. H_β and FeII emission lines are formed in a region much closer to the star than H_α, similar to the classical Be stars in (Hanuschik et al. 1988).

3.3 | Periodogram analysis

The orbital motion of the compact object is expected to produce orbital modulation in the circumstellar disc. A summary of the observed orbital variations in three Be/γ-ray binaries is given in Moritani & Kawachi (2021). To search for signatures of the orbital modulation of the emission lines formed in the Be disc, we conducted a periodogram analysis of the measured emission line parameters (see Section 2) using the phase dispersion minimization, PDM (Stellingwerf 1978), Lomb-Scargle (Lomb 1976; Scargle 1982) and CLEAN (Roberts et al. 1987) algorithms. The analysis was performed using the community-developed core Python package for Astronomy (Astropy Collaboration et al. 2018). The results of the periodogram analysis of EW_α are shown in Figure 4. The CLEAN algorithm shows a prominent peak at 60.43 ± 0.44 days and PDM statistics indicates a minimum at 60.38 ± 0.32 days. The highest peak of Lomb-Scargle is at 60.45 days. The periodogram analysis of H_β parameters gives similar values: 60.3 ± 0.5 days for EW_β and 60.5 ± 0.7 days for ΔV_β. Among the measured parameteres, the orbital period is more clearly visible in EW_α probably because we have 165 measurements in total distributed over 10.5 years.

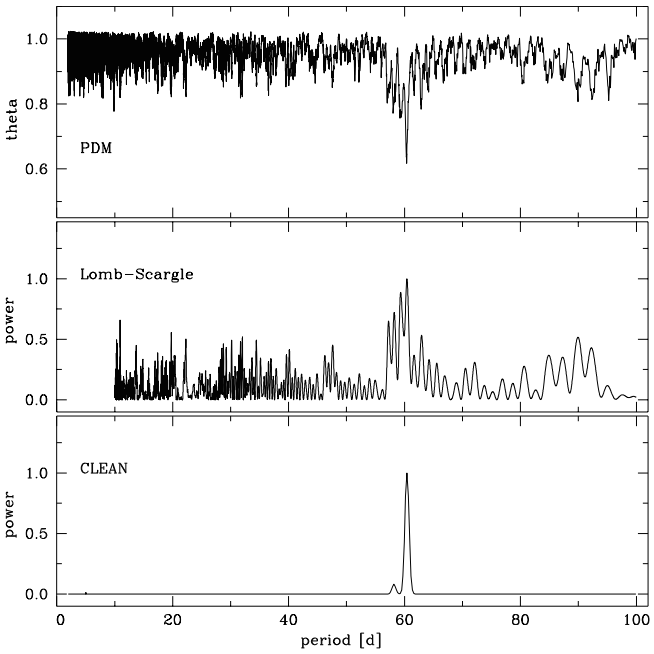

FIGURE 4 Periodogram analysis of EW_α with three independent methods (PDM, Lomb-Scargle and CLEAN). A periodic signal is clearly detected at the orbital period of the binary with PDM and CLEAN algorithms

3.4 | Orbital modulation

Most of the Be/X-ray binaries show an asymmetric double-peaked H_α line, usually caused by a distortion of the density distribution on the disc (Hummel & Hanuschik 1997). The variability of the emission lines is the main indicator for structural changes of the circumstellar disc. The variability of the H_α emission reflects the changes in the outer parts of the disc, while the variability of H_β and FeII emission lines - those in its inner parts. An unperturbed circumstellar disc will produce a double-peaked emission line. In only a few cases in our spectra does the H_α line show two well defined peaks, in others it appears as a single peak, profiles with 3 peaks, and flat top profiles (see the examples in Figure 1). It means distortions of the density distribution in the disc (Hummel & Hanuschik 1997). H_β and FeII lines are always double-peaked in our spectra, which means that the perturbations are stronger in the outer parts of the disc. At distances less than 70 R$_\odot$ (which is approximately the size of the H_β disc) there are no large perturbations. This is in agreement with the supposition of Porter & Rivinius (2003) that in the Be/X-ray binaries the companion has little influence on the Be star and how its disc is produced, but alters only the outer part of the disc.

In Figures 5 and 6 we plot a few parameters folded with the orbital period. We used $P_{\rm orb} = 60.37$ d and $T_0 =$

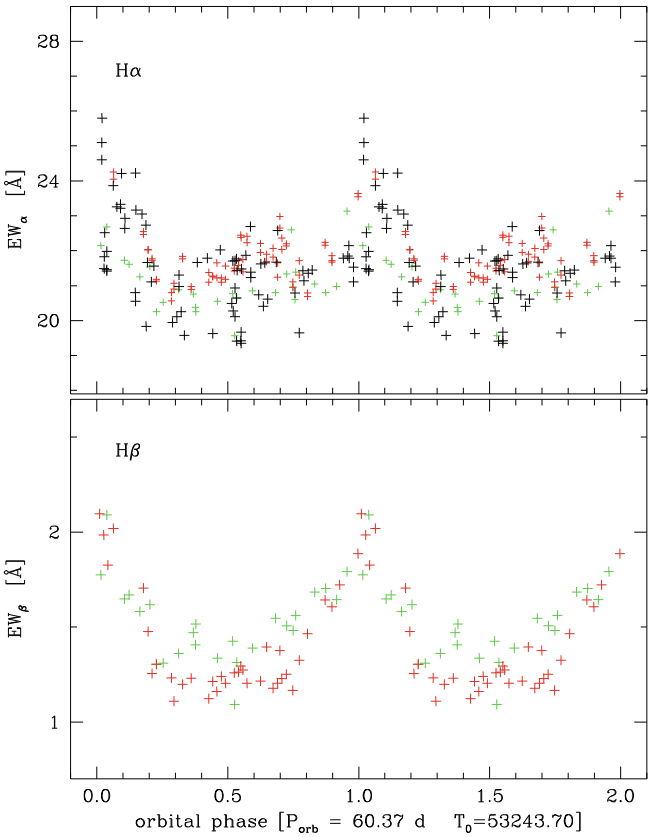

FIGURE 5 Orbital modulation of the equivalent widths of H_α and H_β emissions. In Figures 5 and 6 the folded light curves are shown twice for clarity

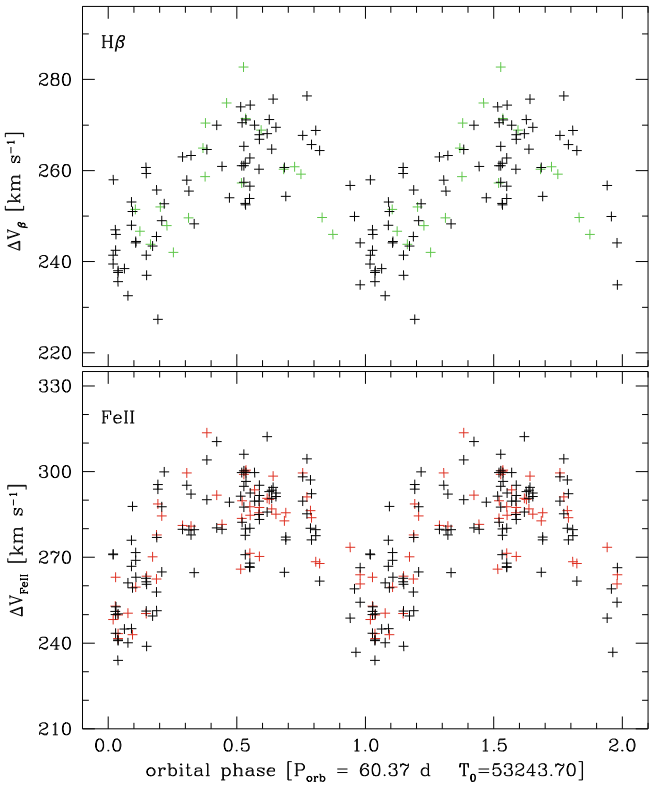

FIGURE 6 Orbital modulation of ΔV_β and $\Delta V_{\rm FeII}$. Clear orbital modulation is visible in Figures 5 and 6, indicating that the disc is larger at periastron (phase 0.0)

53243.70. This ephemeris is from the analysis of the radial velocities (Casares et al. 2014) and the periastron is at phase 0. In each panel the folded light curve is shown twice for clarity. In Figure 5 are plotted the orbital modulation of EW_α and EW_β. The red pluses are the measurements from the Liverpool Telescope spectra, green are TIGRE, and black are Rozhen data. It is clear that the maxima of EW_α and EW_β are around the periastron when the EW_α is about 3 Å larger. When the black hole is at apastron $EW_\beta \approx$ 1.3 Å, while when at periastron it achieves ≈ 2 Å. When the black hole is at apastron $EW_\alpha \approx$ 21 Å, while when at periastron ≈ 24 Å. Using Equation 5, this corresponds to disc size increasing from 136 $R_\odot$ to 151 $R_\odot$. In other words, the size of the H_α disc pulsates with an amplitude of about 15 $R_\odot$ each orbital period. There is no noticeable time delay between the maxima of EW_α and EW_β.

In the upper panel of Figure 6 is plotted the distance between the peaks of the H_β emission line. The black symbols are Rozhen data, the green - TIGRE data. It is clear that ΔV_β is larger at apastron and smaller during the periastron passage. Using Equation 4, we calculate that changes of ΔV_β from 270 to 240 km s^{-1} correspond to changes of the $H\beta$ disc from 47 to 60 $R_\odot$.

In the lower panel of Figure 6 is plotted the variability of FeII lines. This panel contains measurements from the Rozhen spectra only. The black symbols indicate FeII 5316 and FeII 6433; the red, the FeII 5197 line. It is evident that $\Delta V_{\rm FeII}$ is larger at apastron and smaller during the periastron passage. Using Equation 4, we calculate that changes of $\Delta V_{\rm FeII}$ from 300 to 250 km s^{-1} correspond to changes of the FeII disc from 40 to 55 $R_\odot$.

The orbital modulation of the emission lines parameters plotted in Figures 5 and 6 indicates that the disc pulsates with orbital period. The pulsation is visible not only in the outer parts of the disc (H_α), but also in the inner parts (H_β and FeII lines). The relative amplitude of the pulsations is 11% for the H_α emitting disc; 20% for the H_β emitting disc, and 25% for the FeII emitting disc. It seems, that the relative amplitude of the pulsations decreases from the inner toward the outer parts of the disc. Usually the variability of quasi-Keplerian discs of the Be stars has the form of a one-armed global disk oscillation (density and velocity wave) as proposed by Okazaki (1997). What we see in our observations of MWC 656 is something different—pulsations induced by the orbital motion of a black hole.

4 | DISCUSSION

The interaction of the black hole in MWC 656 with the circumstellar disc and the accretion process are expected to be similar to that in the Be/X-ray binaries containing a neutron star. There are two points that we have to bear in mind about the influence of the compact object on the circumstellar disc: (i) a neutron star in a Be/X-ray binary can be in different regimes - accretor, propeller, ejector, georotator, etc. (e.g., Lipunov 1987), while a black hole can only be an accretor, (ii) the black hole is a few times more massive and its influence on the circumstellar disc will consequently be proportionately stronger.

For MWC 656, the orbital plane and the equatorial plane of the mass donor are probably complanar within $\pm 4^0$ (see Section 5 in Zamanov et al. 2021). Following this finding, using inclination $i = 52^0 \pm 2^0$ (Zamanov et al. 2021), and the values of Casares et al. (2014) for the orbital eccentricity $e = 0.1$, and for the semi-major axes $a_1 \sin i = 38.0 \pm 6.3$ R$_\odot$ and $a_2 \sin i = 92.8 \pm 3.8$ R$_\odot$, we find the semi-major axis $a \approx 166$ R$_\odot$ and distance between components at periastron $a(1-e) \approx 149.4$ R$_\odot$ and at apastron $a(1+e) \approx 182.6$ R$_\odot$.

Using the formula by Eggleton (1983) and mass ratio $M_1/M_2 = 2.44$ (Casares et al. 2014), we estimate the dimensionless Roche lobe size $r_L = 0.46$, and thus the Roche lobe size of the primary would be 68 R$_\odot$ and 84 R$_\odot$, for periastron and apastron, respectively. The position of the inner Lagrangian point is at distance 88 R$_\odot$ and 108 R$_\odot$ for periastron and apastron, respectively. This means that the circumstellar disc ($123 \leq R_{\rm disc} \leq 174$ R$_\odot$, Section 3.2) is twice as large as the Roche lobe size and extends beyond the L_1 point.

The interaction between the decretion disc and the neutron star in the Be/X-ray binaries results in truncation of the disc (Okazaki et al. 2002; Okazaki & Negueruela 2001). The observed orbital modulation of the emission lines of MWC 656 probably is due to periodic changes (oscillations) of the truncation radius as a result of the changes of the distance between the components. Other possibilities could be tidal waves induced by the black hole, or changes in the disc border, density, and/or ionization induced by the gravitational force and high energy emission of the black hole.

4.1 | Efficiency of accretion

Typically the B and Be stars have mass loss rate values ranging from 10^{-11} to 3×10^{-9} M$_\odot$ year^{-1} (Snow 1981). More recently Vieira et al. (2017) applied a viscous decretion disc model to the infrared disc continuum emission of 80 Be stars observed in different epochs and estimated the disc mass decretion rates in the range between 10^{-12} and 10^{-9} M$_\odot$ year^{-1}. Rimulo et al. (2018) based on a sample of 54 bright Be stars with clear disc events find the typical mass loss rates associated with the disc events of the order of 10^{-10} M$_\odot$ year^{-1}. It is worth noting that for 28 CMa, Carciofi et al. (2012) find a higher mass injection rate $3.5 \pm 1.3 \times 10^{-8} M_\odot$year^{-1}. Following the above and our results that the circumstellar disc of MWC 656 is similar to the classical Be discs (Figures 2 and 3), we can accept for the primary of MWC 656 a mass loss rate in the range $10^{-9} - 10^{-10}$ M$_\odot$ year^{-1}.

The accretion radius of the black hole is:

$$R_a = \frac{2GM_{\rm BH}}{V_{\rm orb}^2 + c_s^2}, \quad (6)$$

where $V_{\rm orb}$ is the orbital velocity of the black hole and c_s is the speed of sound. We estimate $R_a \approx 250$ R$_\odot$. Having this accretion radius, the black hole will be able to capture approximately 10–30% of the mass loss of the primary. We expect a mass accretion rate onto the black hole to be $10^{-10} - 10^{-11}$ M$_\odot$ year^{-1}. Another estimate can be obtained using the bright Be/X-ray binary X Per, where a 2.07 M$_\odot$ neutron star accretes from a Be star primary at a rate $1.5 \times 10^{-12} - 7 \times 10^{-12}$ M$_\odot$ year^{-1} (Yatabe et al. 2018; Zamanov et al. 2019). Bearing in mind that the orbital period is 4 times shorter and the black hole is 2.5 times more massive, we expect MWC 656 to exhibit at least a 5 times higher mass accretion rate, $7.5 \times 10^{-12} - 3.5 \times 10^{-11}$. Both estimates imply that the most likely mass accretion rate onto the black hole of MWC 656 is $1 - 3 \times 10^{-11}$ M$_\odot$ year^{-1}.

Multiwavelength observations reveal that MWC 656 is a faint X-ray (Munar-Adrover et al. 2014) and radio (Dzib et al. 2015) source. Alexander & McSwain (2016) place upper limits on the gamma-ray emission from this source and point out that it is not likely to be a true gamma-ray binary. Ribo et al. (2017) find that MWC 656 is one of the faintest stellar-mass black holes ever detected in X-rays. The luminosities and the obtained photon index are fully compatible with a black hole in deep quiescence (Plotkin et al. 2013). Ribo et al. (2017) estimated X-ray luminosity $L_X \approx 3 \times 10^{30}$ erg s^{-1} at a 2.6 kpc distance. Using the GAIA eDR3 (Gaia Collaboration et al. 2021) parallax 0.486 mas, the model by Bailer-Jones et al. (2021) provides a distance 1985 pc. We recalculate $L_X \approx 1.75 \times 10^{30}$ erg s^{-1}. The Eddington luminosity is $L_{\rm Edd} = 1.26 \times 10^{38}\, M/{\rm M}_\odot$ erg s^{-1} for ionized Hydrogen. We therefore estimate that the black hole in MWC 656 radiates at $2.8 \times 10^{-9}\, L_{\rm Edd}$.

Following Shakura & Sunyaev (1973) and references therein, the total release of energy during the accretion is $L = \eta \dot{M} c^2$, where η is the efficiency of gravitational energy release; in the case of Schwarzshild's metric $\eta \simeq 0.06$, in

a Kerr black hole η can attain 40%. Supposing that the black hole in MWC 656 accretes at a rate $1-3\times10^{-11}$ $M_\odot$ year^{-1}, we find $\eta \approx 2.10^{-6}$, which is $\sim 3\times10^4$ times lower than expected for a Schwarzshild's metric and indicates that the likely reason the black hole to be in deep quiescence is a very low efficiency of gravitational energy release.

4.2 | Similarity with the Be/neutron star binary PSR B1259-63

PSR B1259-63/LS 2883 is one of the confirmed gamma-ray binary systems, consisting of a 15–31 $M_\odot$ O9.5Ve star and a neutron star, visible as a 47.8 ms radio pulsar (Miller-Jones et al. 2018; Negueruela et al. 2011). The radio observations of the pulsar allow the binary parameters to be well established – 1236.72 d (∼3.4 year) eccentric orbit, with an eccentricity of e = 0.87 (Miller-Jones et al. 2018; Shannon et al. 2014). The spectral observations during three periastron passages (Chernyakova et al. 2014, 2021; Chernyakova et al. 2015) and (van Soelen et al. 2016) reveal an increase of EW_α at the time of the periastron of the neutron star. There is also a hint of a decrease of the distance between the peaks of HeI at the time of the periastron of the neutron star [see Figure 1a in van Soelen et al. 2016 and Figure 1d in Chernyakova et al. 2021]. The behavior of EW_α is very similar during the three periastron passages.

Moreover, during the periastron passage, PSR B1259-63/LS 2883 gets brighter in the NIR bands (Kawachi et al. 2021). The observed increase of the EW_α and NIR variability are likely due to an expansion of the circumstellar disc caused by the tidal force of the compact object.

The behavior of PSR B1259-63/LS 2883 around the periastron resembles our results for MWC 656 – an increase of EW_α and decrease of the ΔV (H_β and FeII) at the periastron (Figures 5 and 6).

4.3 | Comparison with LS I +61303

LS I +61303 is a Be/gamma-ray binary with periodic outbursts and orbital period 26.496 days (Gregory 2002 and references therein). The primary is a B0Ve star. The secondary is most probably a neutron star (Weng et al. 2022), however some models consider the possibility of a black hole (Dzib et al. 2015; Massi et al. 2017). The orbital modulation of H_α is visible in the ratio of the equivalent widths of the blue and red humps, and is an indication of the redistribution of the material in the disc—part of the time there is more material in the blue side and part of the time more material in the red side. The peak of EW_α is not at the periastron, it is in between periastron and apastron (see Figure 1 in Zamanov et al. 2013). This is different from the behavior of PSR B1259-63 and MWC 656.

It is worth noting, that the derived position of the periastron of LS I +61303 is from the orbital solutions of Casares et al. (2005) and Aragona et al. (2009), based on the radial velocities. Some recent models by Kravtsov et al. (2020) and Chen & Takata (2022) cast doubts on the position of the periastron. However, the radial velocity measurements are model independent and more reliable.

The measurements of EW_α of MWC 656 cover 10 years from April 2011 to November 2021. During this decade no big variations of the EW_α are detected, it varies in a relatively narrow range $19.4 \le EW_\alpha \le 25.8$ Å. During 25 years of H_α observations of LS I +61303 also no large variations of the EW_α are observed (Zamanov et al. 2013). In both stars the circumstellar disc is stable and no episode of disc loss is observed. A difference is that in LS I +61303 the H_α emission is always double-peaked, while in MWC 656 it is double-peaked on only a few occasions, which means that it is perturbed. A possible reason can be that in MWC 656 the black hole is more massive than the neutron star in LS I +61303.

We note in passing, that it will be interesting to study the inner disc of LS I +61303, which probably is seen in H_β and H_γ lines and to observe PSR B1259-63 during one or two entire orbital periods.

5 | CONCLUSIONS

We analyzed 165 spectra of the Be/black hole binary MWC 656 obtained with Rozhen, TIGRE and Liverpool telescopes during the period April 2011–October 2021. We studied the orbital modulation of the H_α, H_β, and FeII emission lines, which are formed in the Be circumstellar disc. The orbital modulations of the emission lines suggest pulsations in the circumstellar disc induced by the orbital motion of the black hole. The overall structure of the circumstellar disc is similar to that of the Be stars and the reason the black hole in MWC 656 appears to be in deep quiescence is probably a very low efficiency of accretion.

ACKNOWLEDGMENTS

This work was supported by the Bulgarian National Science Fund *project* KP-06-H28/2 08.12.2018 "Binary stars with compact object". TIGRE is a collaboration of the Hamburger Sternwarte, the Universities of Hamburg, Guanajuato and Liege. Liverpool Telescope is operated on the island of La Palma by Liverpool John Moores University in the Spanish Observatorio del Roque de los Muchachos of the Instituto de Astrofisica de Canarias with financial support from the UK STFC. DM acknowledges support from the Research Fund of the Shumen University.

FUNDING INFORMATION

Bulgarian National Science Fund, project KP-06-H28/2 08.12.2018 “Binary stars with compact object”.

CONFLICT OF INTERESTS

The authors declare no potential conflict of interests.

REFERENCES

Aleksić, J., Ansoldi, S., Antonelli, L. A., et al. 2015, *A&A*, *576*, A36.

Alexander, M. J., & McSwain, M. V. 2016, *Gamma-ray Observations*. in: *Bright Emissaries: Be Stars as Messengers of Star-Disk Physics*, eds. T. A. A. Sigut & C. E. Jones, ASP Conference Series, San Francisco, Vol. *506*, 243.

Andrillat, Y. 1983, *A&AS*, *53*, 319.

Aragona, C., McSwain, M. V., Grundstrom, E. D., et al. 2009, *ApJ*, *698*(1), 514.

Astropy Collaboration, Price-Whelan, A. M., Sipőcz, B. M., et al. 2018, *AJ*, *156*(3), 123.

Bailer-Jones, C. A. L., Rybizki, J., Fouesneau, M., Demleitner, M., & Andrae, R. 2021, *AJ*, *161*(3), 147.

Bonev, T., Markov, H., Tomov, T., et al. 2017, *Bulg Astron J*, *26*, 67.

Brandt, N., & Podsiadlowski, P. 1995, *MNRAS*, *274*(2), 461.

Brown, R. O., Coe, M. J., Ho, W. C. G., & Okazaki, A. T. 2019, *MNRAS*, *488*(1), 387.

Brown, R. O., Ho, W. C. G., Coe, M. J., & Okazaki, A. T. 2018, *MNRAS*, *477*(4), 4810.

Carciofi, A. C., Bjorkman, J. E., Otero, S. A., et al. 2012, *ApJ*, *744*(1), L15.

Casares, J., Negueruela, I., Ribo, M., Ribas, I., Paredes, J. M., Herrero, A., & Simon-Diaz, S. 2014, *Nature*, *505*(7483), 378.

Casares, J., Ribas, I., Paredes, J. M., Marti, J., & Allende Prieto, C. 2005, *MNRAS*, *360*(3), 1105.

Casares, J., Ribo, M., Ribas, I., Paredes, J. M., Vilardell, F., & Negueruela, I. 2012, *MNRAS*, *421*(2), 1103.

Catanzaro, G. 2013, *A&A*, *550*, A79.

Chen, A. M., & Takata, J. 2022, *A&A*, *658*, A153.

Chernyakova, M., Abdo, A. A., Neronov, A., et al. 2014, *MNRAS*, *439*(1), 432.

Chernyakova, M., Malyshev, D., van Soelen, B., et al. 2021, *Universe*, *7*(7), 242.

Chernyakova, M., Neronov, A., van Soelen, B., et al. 2015, *MNRAS*, *454*(2), 1358.

Coe, M. J., Reig, P., McBride, V. A., Galache, J. L., & Fabregat, J. 2006, *MNRAS*, *368*(1), 447.

Dachs, J., Hummel, W., & Hanuschik, R. W. 1992, *A&AS*, *95*, 437.

Dzib, S. A., Massi, M., & Jaron, F. 2015, *A&A*, *580*, L6.

Eggleton, P. P. 1983, *ApJ*, *268*, 368.

Gaia Collaboration,Brown, A. G. A., Vallenari, A., et al. 2021, *A&A*, *649*, A1.

Gregory, P. C. 2002, *ApJ*, *575*(1), 427.

Hanuschik, R. W. 1986, *A&A*, *166*, 185.

Hanuschik, R. W., Kozok, J. R., & Kaiser, D. 1988, *A&A*, *189*, 147.

Heiselberg, H., & Pandharipande, V. 2000, *Ann Rev Nucl Part Sci*, *50*, 481.

Huang, S.-S. 1972, *ApJ*, *171*, 549.

Hummel, W. 1994a, *Ap&SS*, *216*(1–2), 87.

Hummel, W. 1994b, *A&A*, *289*, 458.

Hummel, W., & Hanuschik, R. W. 1997, *A&A*, *320*, 852.

Kawachi, A., Moritani, Y., Okazaki, A. T., Yoshida, H., & Suzuki, K. 2021, *PASJ*, *73*(3), 545.

Kravtsov, V., Berdyugin, A. V., Piirola, V., et al. 2020, *A&A*, *643*, A170.

Lipunov, V. M. 1987, *Ap&SS*, *132*(1), 1.

Lomb, N. R. 1976, *Ap&SS*, *39*(2), 447.

Lucarelli, F., Verrecchia, F., Striani, E., et al. 2010, *Astronom Teleg*, *2761*, 1.

Martin, R. G., Tout, C. A., & Pringle, J. E. 2009, *MNRAS*, *397*(3), 1563.

Massi, M., Migliari, S., & Chernyakova, M. 2017, *MNRAS*, *468*(3), 3689.

Miller-Jones, J. C. A., Deller, A. T., Shannon, R. M., et al. 2018, *MNRAS*, *479*(4), 4849.

Monageng, I. M., McBride, V. A., Coe, M. J., Steele, I. A., & Reig, P. 2017, *MNRAS*, *464*(1), 572.

Morales-Rueda, L., Carter, D., Steele, I. A., Charles, P. A., & Worswick, S. 2004, *Astronomische Nachrichten*, *325*(3), 215.

Moritani, Y., & Kawachi, A. 2021, *Universe*, *7*(9), 320.

Munar-Adrover, P., Paredes, J. M., Ribo, M., Iwasawa, K., Zabalza, V., & Casares, J. 2014, *ApJ*, *786*(2), L11.

Negueruela, I. 2007, January, *Be/X-ray Binaries: An Observational Approach*. in: *Massive Stars in Interactive Binaries*, eds. N. St. -Louis & A. F. J. Moffat, ASP Conference Series, San Francisco, Vol. *367*, 477.

Negueruela, I., Ribo, M., Herrero, A., Lorenzo, J., Khangulyan, D., & Aharonian, F. A. 2011, *ApJ*, *732*(1), L11.

Nice, D. J., Splaver, E. M., Stairs, I. H., Lohmer, O., Jessner, A., Kramer, M., & Cordes, J. M. 2005, *ApJ*, *634*(2), 1242.

Okazaki, A. T. 1997, *A&A*, *318*, 548.

Okazaki, A. T., Bate, M. R., Ogilvie, G. I., & Pringle, J. E. 2002, *MNRAS*, *337*(3), 967.

Okazaki, A. T., & Negueruela, I. 2001, *A&A*, *377*, 161.

Peters, G. J., Pewett, T. D., Gies, D. R., Touhami, Y. N., & Grundstrom, E. D. 2013, *ApJ*, *765*(1), 2.

Plotkin, R. M., Gallo, E., & Jonker, P. G. 2013, *ApJ*, *773*(1), 59.

Pols, O. R., Cote, J., Waters, L. B. F. M., & Heise, J. 1991, *A&A*, *241*, 419.

Porter, J. M., & Rivinius, T. 2003, *PASP*, *115*(812), 1153.

Reig, P. 2011, *Ap&SS*, *332*(1), 1.

Ribo, M., Munar-Adrover, P., Paredes, J. M., et al. 2017, *ApJ*, *835*(2), L33.

Rimulo, L. R., Carciofi, A. C., Vieira, R. G., et al. 2018, *MNRAS*, *476*(3), 3555.

Rivinius, T., Carciofi, A. C., & Martayan, C. 2013, *A&A Rev*, *21*, 69.

Roberts, D. H., Lehar, J., & Dreher, J. W. 1987, *AJ*, *93*, 968.

Scargle, J. D. 1982, *ApJ*, *263*, 835.

Schmitt, J. H. M. M., Schroder, K. P., Rauw, G., et al. 2014, *Astronomische Nachrichten*, *335*(8), 787.

Shakura, N. I., & Sunyaev, R. A. 1973, *A&A*, *24*, 337.

Shannon, R. M., Johnston, S., & Manchester, R. N. 2014, *MNRAS*, *437*(4), 3255.

Shao, Y., & Li, X.-D. 2020, *ApJ*, *898*(2), 143.

Shibata, M., Zhou, E., Kiuchi, K., & Fujibayashi, S. 2019, *Phys Rev D*, *100*(2), 23015.

Slettebak, A., Collins, I., George, W., & Truax, R. 1992, July, *ApJS*, *81*, 335.
Snow, J. 1981, *ApJ*, *251*, 139.
Steele, I. A., Smith, R. J., Rees, P. C., et al. 2004, *Proc. SPIE*, *5489*, 679.
Stellingwerf, R. F. 1978, *ApJ*, *224*, 953.
van Soelen, B., Vaisanen, P., Odendaal, A., Klindt, L., Sushch, I., & Meintjes, P. J. 2016, *MNRAS*, *455*(4), 3674.
Vieira, R. G., Carciofi, A. C., Bjorkman, J. E., Rivinius, T., Baade, D., & Rimulo, L. R. 2017, *MNRAS*, *464*(3), 3071.
Weng, S.-S., Qian, L., Wang, B.-J., et al. 2022, *Nat Astron*. in press
Williams, S. J., Gies, D. R., Matson, R. A., Touhami, Y., Grundstrom, E. D., Huang, W., & McSwain, M. V. 2010, *ApJ*, *723*(1), L93.
Yatabe, F., Makishima, K., Mihara, T., et al. 2018, *PASJ*, *70*(5), 89.
Zamanov, R., Stoyanov, K., Marti, J., Tomov, N. A., Belcheva, G., Luque-Escamilla, P. L., & Latev, G. 2013, *A&A*, *559*, A87.
Zamanov, R., Stoyanov, K. A., Wolter, U., Marchev, D., & Petrov, N. I. 2019, *A&A*, *622*, A173.
Zamanov, R. K., Stoyanov, K. A., Mart, J., Marchev, V. D., & Nikolov, Y. M. 2021, *Astronomische Nachrichten*, *342*(3), 531.
Zamanov, R. K., Stoyanov, K. A., Marti, J., Latev, G. Y., Nikolov, Y. M., Bode, M. F., & Luque-Escamilla, P. L. 2016, *A&A*, *593*, A97.

AUTHOR BIOGRAPHY

Radoslav K. Zamanov: MSc - Sofia University St. Kl. Ohridski (1989); PhD - National Astronomical Observatory Rozhen, Bulgaria (1997); fellow - Universidad de Jaen, Spain (2000); postdoc - Osservatorio Astronomico di Padova, Padova, Italy (2001–2003); postdoc research assistant - Astrophysics Research Institute, Liverpool John Moores University, UK (2003–2005); proffesor of astrophysics and stellar astronomy - Institute of Astronomy and NAO, Bulgarian Academy of Sciences (since 2012).

SUPPORTING INFORMATION

Additional supporting information can be found online in the Supporting Information section at the end of this article.

How to cite this article: Zamanov, R. K., Stoyanov, K. A., Marchev, D., et al. 2022, *Astron. Nachr.*, e20224019. https://doi.org/10.1002/asna.20224019